Computational Evaluation of an OML-based Heat Exchanger Concept for HEATheR

Emre Sozer*
Daniel Maldonado†

NASA Ames Research Center, Moffett Field, CA 94035

Keerti Bhamidipati‡

NASA Armstrong Flight Research Center, Edwards, CA 93523

Sydney L. Schnulo§

NASA Glenn Research Center, Cleveland, OH 44135

Feasibility of outer mold line (OML) heat exchangers for electrified aircraft is computationally explored for three different aircraft concepts within The High-efficiency Electrified Aircraft Thermal Research (HEATheR) project. OML surface temperature limits were selected based on aluminum-alloy and carbon-fiber composite materials commonly used in transport aircraft. Heat flux distribution over the aircraft OML at the surface temperature limit was evaluated with computational fluid dynamics (CFD) analysis. The candidate OML locations and the size for the implementation of the OML-based heat exchanger is down-selected using this initial analysis and other considerations including the concern for structural integrity and proximity to heat-generating electrical components. The sensitivity of the heat transfer analysis to the computational grid, aircraft angle of attack, surface temperature, and the interaction of individual OML heat exchanger patches were investigated.

I.   Introduction

The High-efficiency Electrified Aircraft Thermal Research (HEATheR) project addresses a major challenge in electrified aircraft propulsion (EAP): thermal management. EAP powertrains have electric components that are often over 90 percent efficient, much higher than traditional gas turbine and piston engine systems. Also unlike piston and turbine engines, the heat that must be rejected is at low rejection temperatures because of the limits of the electric components. The traditional engines also have the advantage of wasting heat directly into their exhaust. Electric components do not have this kind of mechanism of heat exhaustion, so they must rely on more complex thermal management systems (TMS). Current thermal management systems being considered for EAP include traditional heat exchangers on pumped fluid loops. These thermal management systems penalize the aircraft performance in terms of power draw, drag, and weight.[1] They require an additional power draw in order to run the fluid pumps. Any ducted air through the TMS may incur a drag penalty when going through the pressure drop over the heat exchangers. Finally, the aircraft performance is affected by the weight of the TMS components: the fluid lines, pumps, fans, and heat exchangers.

The HEATheR project considers whether reducing these heat loads by increasing the efficiency of the powertrain can enable a more favorable TMS. This is partially inspired by the high lift motor controller

*Computational Aerosciences Branch, emre.sozer@nasa.gov
†Science and Technology Corporation, daniel.maldonado@nasa.gov
‡Aerostructures Branch, keerti.k.bhamidipati@nasa.gov
§Propulsion System Analysis Branch, sydney.l.schnulo@nasa.gov

American Institute of Aeronautics and Astronautics

(HLMC) design for NASA's fully electric experimental aircraft, the X-57 Maxwell. The 11 kW HLMC demonstrated adequate cooling by sinking the heat through the outer mold line (OML) of the motor nacelle.[2] The high efficiency of the motor controller enabled this minimally penalizing approach to thermal management. Because the OML was not changed, thermal management did not add any drag penalty. The entirely passive architecture eliminated any power requirements, and added weight was minimal due to the low heat load.

HEATheR is investigating the feasibility of OML cooling for 3 separate EAP concepts. The first is a Single-aisle Turboelectric AiRCraft with Aft Boundary Layer ingesting propulsion (STARC-ABL, Figure 1). This is a 150-passenger concept that uses a 3500 hp fan at the aft of the fuselage to re-accelerate the boundary layer for a fuel burn benefit.[3] The boundary layer ingesting fan is driven by an electric motor, which gets its energy from generators on the low-pressure shaft of the underwing turbofans.

Figure 1: Single Aisle Turboelectric Aircraft concept (STARC-ABL).

The second concept, shown in Figure 2, is the Revolutionary Vertical Lift Technologies (RVLT) project's 15 passenger tiltwing concept.[4] This is a turboelectric Urban Air Mobility (UAM) concept vehicle with one turboshaft engine that drives a generator to power the 4 fans along the leading edge of the wing.

Figure 2: Revolutionary Vertical Lift Technologies (RVLT) 15 passenger tiltwing concept.

Finally, we consider the Parallel Electric-Gas Architecture with Synergistic Utilization Scheme (PEGASUS) vehicle,[5] as displayed in Figure 3. This vehicle is a 48-passenger hybrid electric concept that has a shorter range, 200 nm, fully electric mission and a turboelectric architecture for longer range missions.

Figure 3: Parallel Electric-Gas Architecture with Synergistic Utilization Scheme (PEGASUS) Concept.

American Institute of Aeronautics and Astronautics

Feasibility of OML-based cooling is assessed for all three vehicles with a multi-step approach. Initially OML surface temperature limits were selected based on aluminum-alloy and carbon-fiber composite materials commonly used in transport aircraft. Using these surface temperature limits as an isothermal condition for OML, an initial CFD simulation of the aircraft was conducted to obtain the distribution of heat flux over the OML. Then candidate locations and sizing of the OML locations are narrowed down with considerations of proximity to electrical components, structural integrity and ease of implementation. An updated CFD simulation was performed with only the down-selected OML cooling patches active. Finally, the sensitivity of the simulations were assessed for variations of flight conditions, surface temperature, computational grid and angle of attack. In addition to the OML cooling capacity, the CFD simulations also offered an insight into the effects of OML cooling on aerodynamic forces.

CFD simulation results, used in conjunction with powertrain component waste heat loads and component maximum temperatures, provided surface area required for rejecting heat at the candidate OML cooling locations. Since only ~10% of the aircraft OML would be required to reject electric-powertrain waste heat, an approach of locating a dedicated OML cooling patch close to each component was selected. It was assumed a next-generation transport aircraft would have a carbon-fiber composite external skin. Since carbon-fiber skin has poor out-of-plane thermal conductivity, a skin cut-out and replacement with an aluminum patch was presumed to transport heat to the external ambient air. OML cooling patch area sizes were translated to weight penalty estimates using skin cut-out aircraft structural design methods. Weight penalty estimates included weights for the: (1) structure required to restore aircraft strength, (2) conductive cooling surface exposed to the external air, and (3) mechanism used to transport component heat to the conductive surface.

II.   Computational Method

The LAVA (Launch Ascent and Vehicle Aerodynamics) solver[6–9] is a CFD framework consisting of three main components, providing capability to operate with various grid paradigms and discretizations that are best suited to simulation needs. The first component is LAVA-Cartesian, a block-structured, immersed boundary Cartesian discretization with Adaptive Mesh Refinement (AMR) capability. This Cartesian based approach is beneficial when highly complex geometries are considered, requiring only a closed surface triangulation for automatic grid generation. The second component is LAVA-Unstructured, an unstructured finite volume discretization, which can be utilized to model high-Reynold number flows with body fitted meshes that can be created with little manual effort. The third component is LAVA-Curvilinear, a structured curvilinear grid method with overset communication. This component may require a larger labor investment when creating grids around complex geometries but it offers a fast solution turn-around time.

For the HEATheR OML heat transfer analysis, LAVA unstructured is utilized in order to quickly model the three different aircraft concepts. LAVA-unstructured solves the compressible Reynolds Averaged Navier-Stokes (RANS) equations on unstructured grids consisting of arbitrary polyhedral cells. A 2nd order finite-volume cell-centered discretization is utilized with MUSCL reconstruction and minmod limiter. Interface fluxes are computed using HR-SLAU2[10] flux function. Viscous fluxes are discretized with a 2nd order accurate scheme and the turbulence is modeled using the Spalart-Allmaras one-equation model (SA).[11, 12]

Steady state solutions are carried out by implicit marching in pseudo time, where each unstructured cell utilizes a local pseudo-time step size determined by a local CFL condition. The local CFL for each cell is further controlled by a robust, adaptive algorithm that monitors the evolution of the solution. The assembled linear system is solved using a GMRES algorithm.

The propulsors are modeled using an actuator zone model, where the thrust and torque due to the propulsors are applied to the flow field as uniform momentum and energy sources over a finite volumetric zone covering the zone traveled by the propeller blades, or the gas flow path of in the case of jet engines.

III.   Results

III.A.   STARC-ABL

An arbitrary polyhedral unstructured grid containing 25.6 million cells was generated for the STARC-ABL (see Figure 4). The grid employs polygonal prisms near the walls with an initial wall normal spacing of $y^+ < 1$ to resolve the boundary layer.

Half of the airplane was modeled, taking advantage of the symmetry. The nacelles were modeled as

American Institute of Aeronautics and Astronautics

flow-through, and the under-wing pylons were omitted due to the lack of clean geometry definition at the time. The aircraft surface was split into patches, as shown in Figure 5, in order to assess patch-averaged, as well as continuous distribution of heat flux. The wing surfaces were split at 1/4 and 3/4 chord locations, approximately corresponding with the spars.

Surface temperature was taken as 200°F, which was found to be a viable skin temperature for long-term service under tensile stress for both aluminum or composite skins. The initial simulation for STARC-ABL used an isothermal wall boundary condition at 200°F temperature over the entire aircraft OML. This was done to gain a preliminary insight into the heat flux distribution, and to narrow down the location and size of the OML cooling patches in the final concept design.

The aircraft was assumed to cruise at an altitude of $h = 37280 ft$, with $Mach = 0.785$. For take-off, an altitude of $h = 0$ with $Mach = 0.2547$ was used. The ambient temperature for take-off was assumed to be 18°F hotter than standard atmosphere value, a conservative approach since OML heat rejection will be more difficult. A range of angle of attacks was simulated for both cruise and take-off.

The preliminary simulations for STARC-ABL were conducted with all propulsors off (with flow-through geometry). Final simulations for the vehicle, used for the sizing of the OML heat exchanger design, included the effect of the propulsors using the actuator zone model as described in Section II.
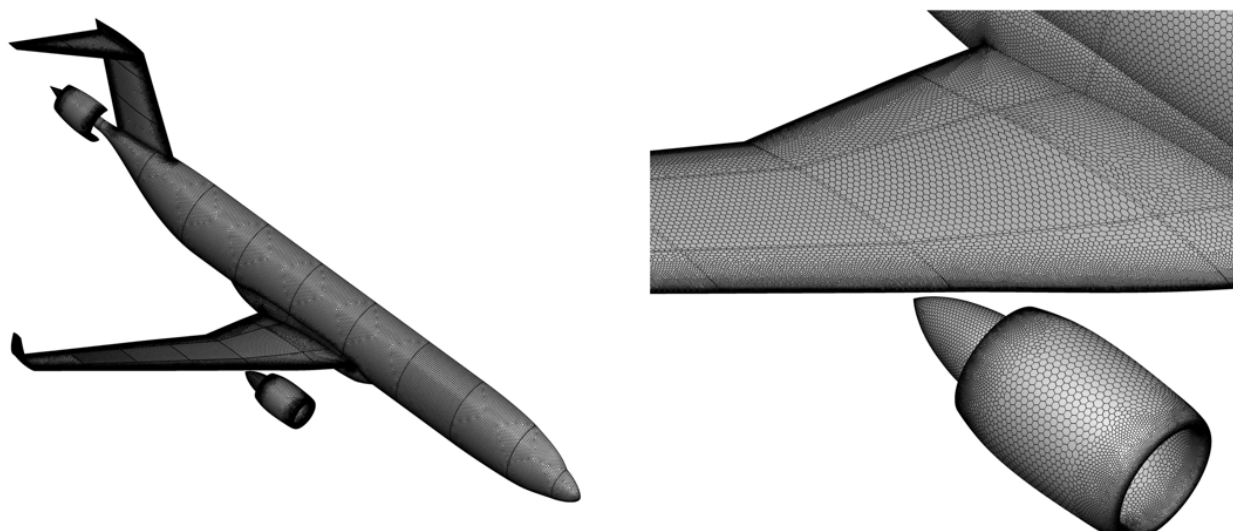

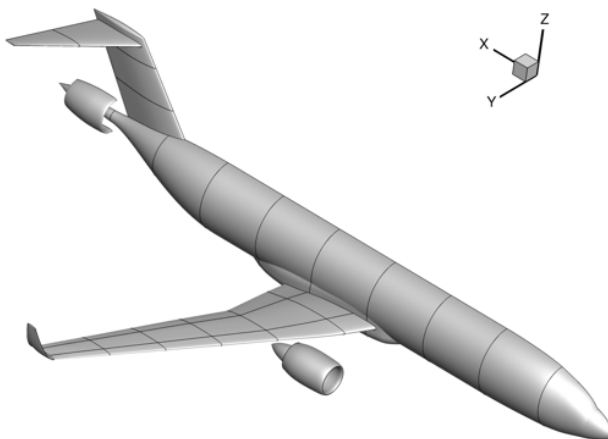Figure 4: Arbitrary polyhedral unstructured grid for STARC-ABL.

Figure 5: STARC-ABL surface splitting.

III.A.1. Preliminary Results

Figures 6 and 7 show the continuous (left) and patch-averaged (right) heat flux distribution for STARC-ABL at cruise conditions. The patches with high heat flux indicate a high heat rejection capacity. A number of observations can immediately be made:

- On the wing, the leading edge, upper-wing trailing edge, and the lower-wing mid-chord section stand out to offer high heat rejection capacity at cruise. The trailing edge houses the control surfaces and is not deemed to be the best choice for the implementation of OML-based heat exchanger. The leading edge is a possibility but the lower-wing mid-chord section would be the first choice since it is under tensile stress (less affected by operation at high temperature), it is in close proximity to under-wing generator components and the system can be implemented relatively easily at this location.

- On the fuselage, the heat rejection capacity seems to be the highest at the nose and lower towards aft as expected. However, the nose is impractical to implement the OML cooling system due to the distance from electrical components. We further limit the choice to the lower half of the fuselage due to structural integrity concerns. These considerations narrow down candidate locations on the fuselage to the lower-aft portion. Unfortunately, those locations correspond to the lower performing sections on the fuselage in terms of heat transfer. Please note that at this initial stage of analysis, the propulsors were off, hence we are not benefiting from any potential boundary layer acceleration effect that the tail cone thrustor may provide. This effect of propulsion will be explored in proceeding analysis.

- Tail surfaces and nacelles may also be viable choices and can be considered if the wing and fuselage choices don't lead to a sufficient system.
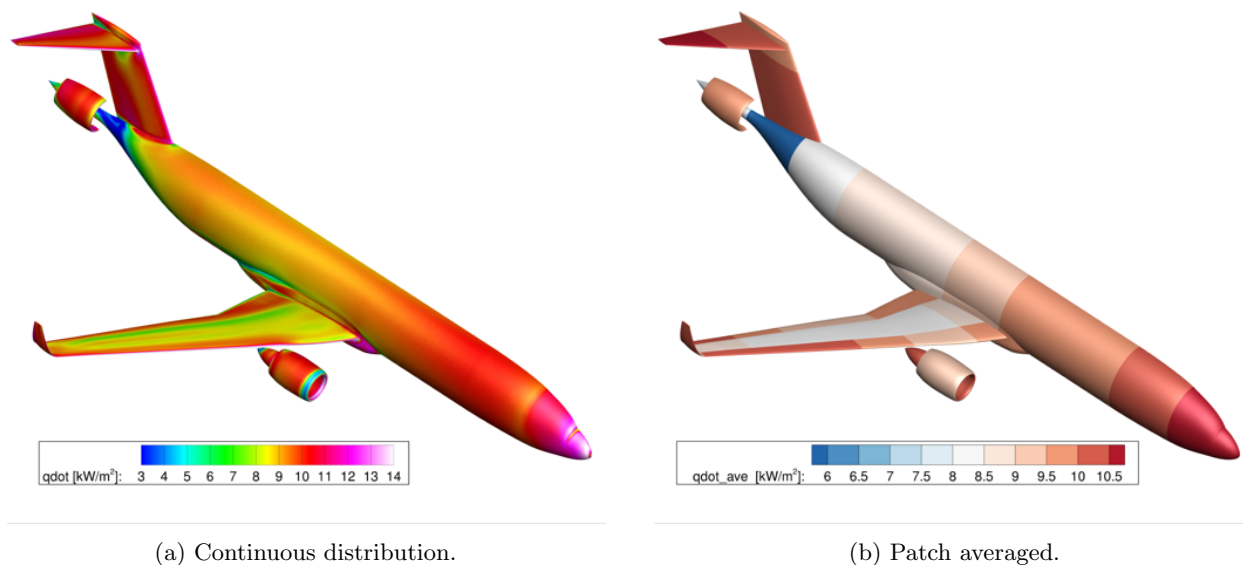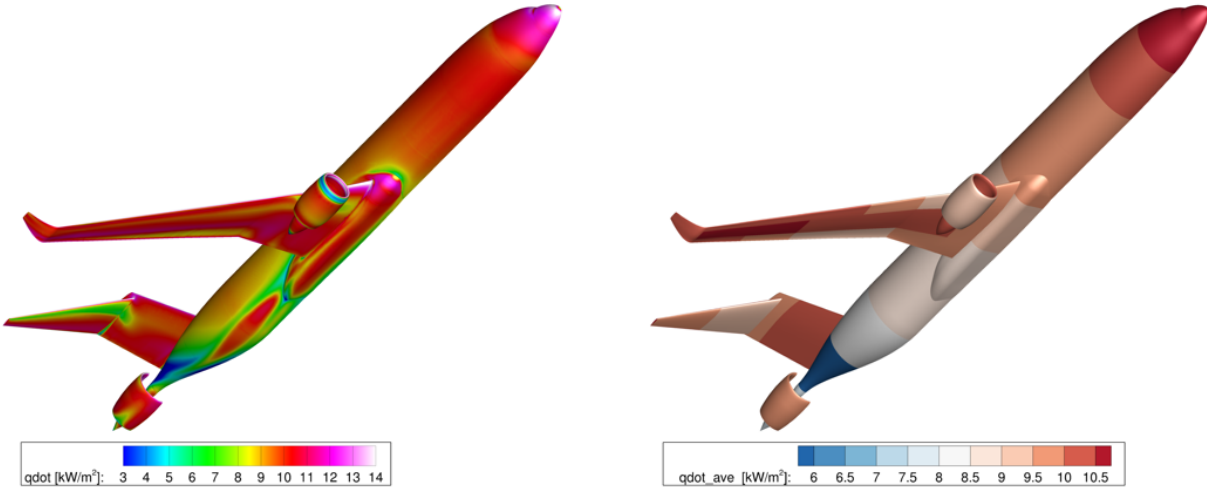

(a) Continuous distribution.

(b) Patch averaged.

Figure 6: Heat flux through the entire STARC-ABL OML at cruise conditions with $\alpha = 0°$ (top view).

The heat transfer distribution at take-off is shown in Figures 8 and 9 for an angle of attack of $\alpha = 8°$. Please note that in reality, the take-off condition is only a transient state and will not be sustained for any significant length of time for the heat transfer to become steady state. So, the takeaway from this simulation is to inspect if there is any significant decay in potential heat transfer rates due to reduced flow speed and increased ambient temperature. This, however, doesn't seem to be the case thanks to compensation by increased air density. We do in fact observe an increased heat transfer rate at the upper leading edges, because of the acceleration at the high angle of attack.

*III.A.2. Angle of Attack Sensitivity*

Figure 10 demonstrates the sensitivity of heat rejection over two different OML patches to the angle of attack for both cruise and take-off conditions. Please note that the sensitivity for other patches were investigated

(a) Continuous distribution.

(b) Patch averaged.

Figure 7: Heat flux through the entire STARC-ABL OML at cruise conditions with $\alpha = 0°$ (bottom view).
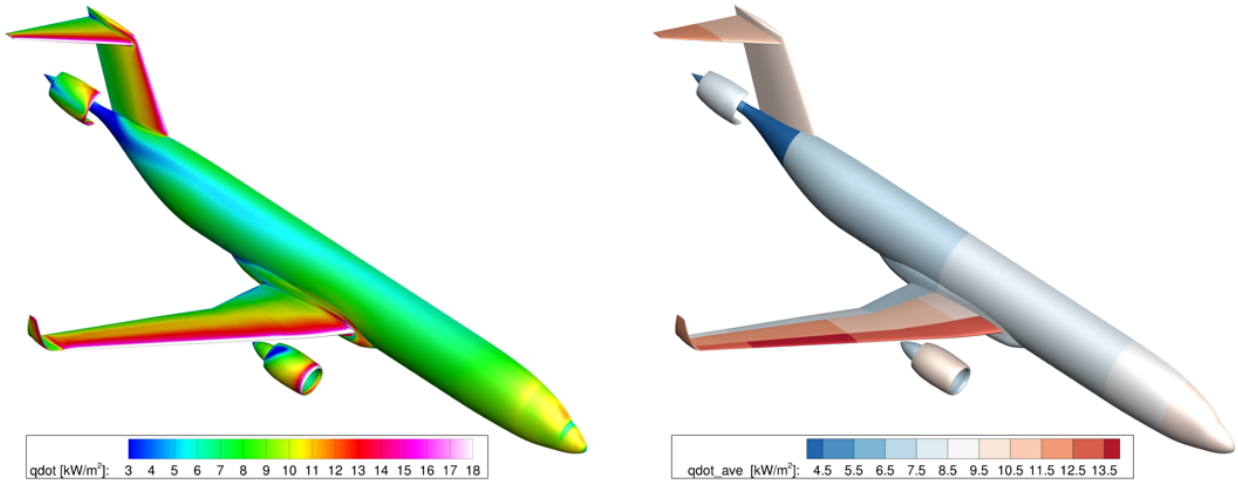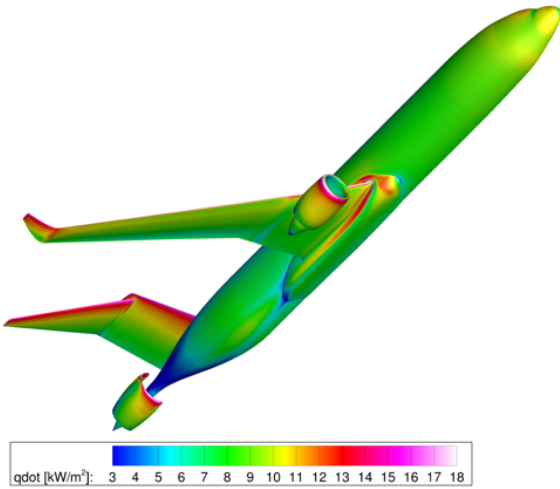

(a) Continuous distribution.

(b) Patch averaged.

Figure 8: Heat flux through the entire STARC-ABL OML at take-off conditions with $\alpha = 8°$ (top view).

as well, but not shown here for the sake of brevity. The wing patches shown here, however, represent some of the largest sensitivities observed. Particularly a sharp drop-off of heat transfer rate can be observed for wing-upper inboard section at high angle of attack take-off conditions, an expected behavior indicating stall. Conversely, the same isn't true for the wing-lower mid-board section where the heat transfer stays largely insensitive to angle of attack at take-off conditions, even for high angle of attacks. This also supports the choice of the wing-lower section as a viable candidate of OML cooling implementation. At cruise condition, the wing-lower patch exhibits an approximately $\sim \pm 10\%$ sensitivity with an angle of attack variation range of $\pm 4°$.

III.A.3. *Grid Sensitivity*

The sensitivity of the STARC-ABL simulations with respect to spatial discretization is investigated with a grid refinement study. The simulations at cruise condition is repeated with 2 additional levels of overall

(a) Continuous distribution.
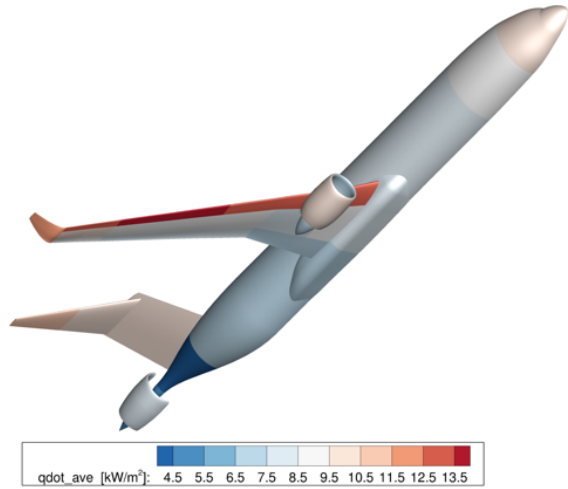
(b) Patch averaged.

Figure 9: Heat flux through the entire STARC-ABL OML at take-off conditions with $\alpha = 8°$ (bottom view).
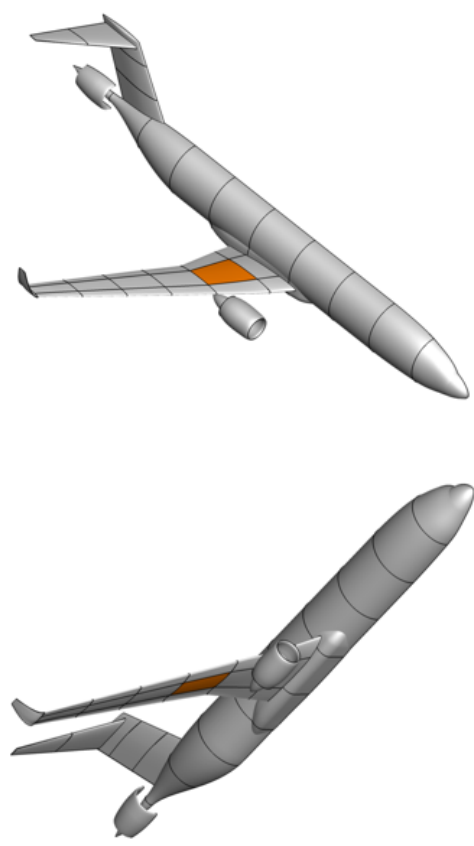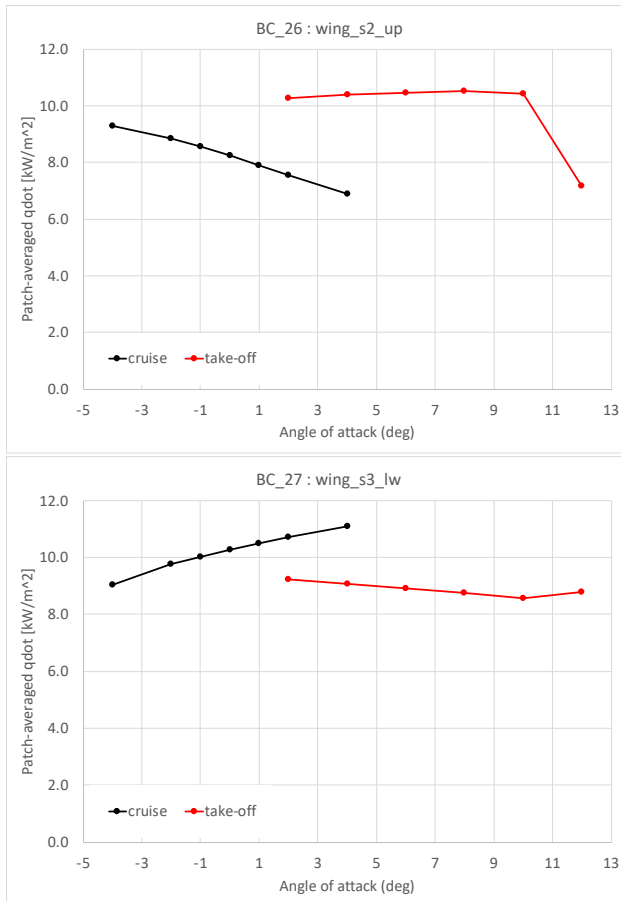

Figure 10: Sensitivity of patch-averaged heat flux for STARC-ABL.

refinement, reducing the cell spacing by factors of 0.75x and 0.5x consecutively. Note that the refinement is applied as consistently as possible within the unstructured mesh generation paradigm. In addition, a separate refinement study looked at the effect of halving the wall wall normal spacing, reducing the y^+

American Institute of Aeronautics and Astronautics

further and tightening the normal spacing in the boundary layers. The results of the grid sensitivity is shown in Figure 11. The patch-averaged heat flux results are affected by less than 3% for all 3 refinements, and the current grid resolution is found to be sufficient.

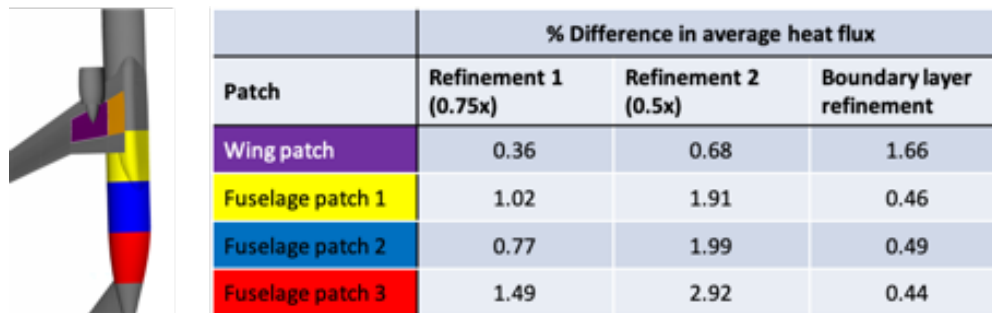| Patch	% Difference in average heat flux		
	Refinement 1 (0.75x)	Refinement 2 (0.5x)	Boundary layer refinement
Wing patch	0.36	0.68	1.66
Fuselage patch 1	1.02	1.91	0.46
Fuselage patch 2	0.77	1.99	0.49
Fuselage patch 3	1.49	2.92	0.44

Figure 11: STARC-ABL grid sensitivity results.

Based on the observations as discussed above, an updated unstructured grid was prepared with a focus on the down-selected OML cooling candidate patches as seen in Figure 12. The updated grid contains 28.5 million polyhedral elements, slightly more than the original grid utilized, due to the increased resolution at patch boundaries. In the following simulations with the updated patch splitting, only the highlighted patches are considered as isothermal heat transfer surfaces while the rest of the aircraft OML is modeled as adiabatic surfaces.
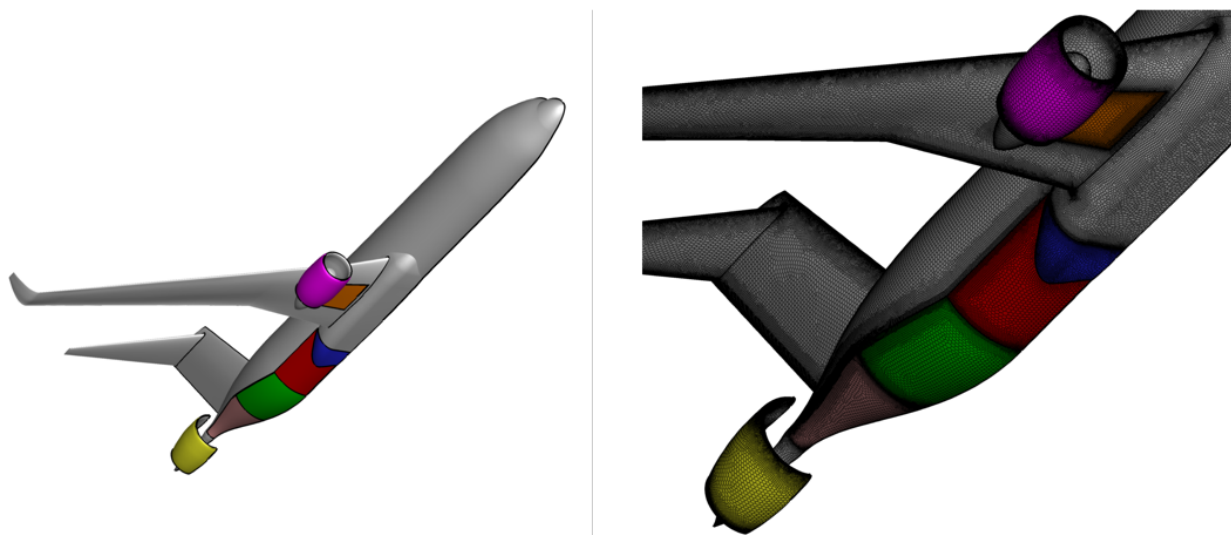

Figure 12: Updated STARC-ABL surface grid with the down-selected candidate OML cooling patches.

III.A.4.   OML Cooling Patch Interactions

Figures 13 through 15 demonstrate the sensitivity of patch-averaged heat flux with respect to patch-to-patch interactions. In the figures, each configuration is illustrated with the active heat transfer patches highlighted in red (the rest of the aircraft surface is taken as adiabatic). In Figure 13, we observe that the average cooling over the wing-lower patch and the under wing nacelle patch have virtually no effect on each other. Figures 14 and 15 shows the interaction between aft fuselage patches. Fuselage patches 1 through 3, listed in plot titles correspond to the patches from the foremost to the aftmost in order. For the patches 1 and 2 (Figure 14), the interaction with the other patches are minimal, with the highest difference being $\sim 4\%$. For the aftmost fuselage patch (Figure 15), the interaction with the patches upstream of it is much more significant, yielding a $\sim 14\%$ capacity loss while the patch 2 is active and $\sim 18\%$ loss while both patches 1 and 2 are active.
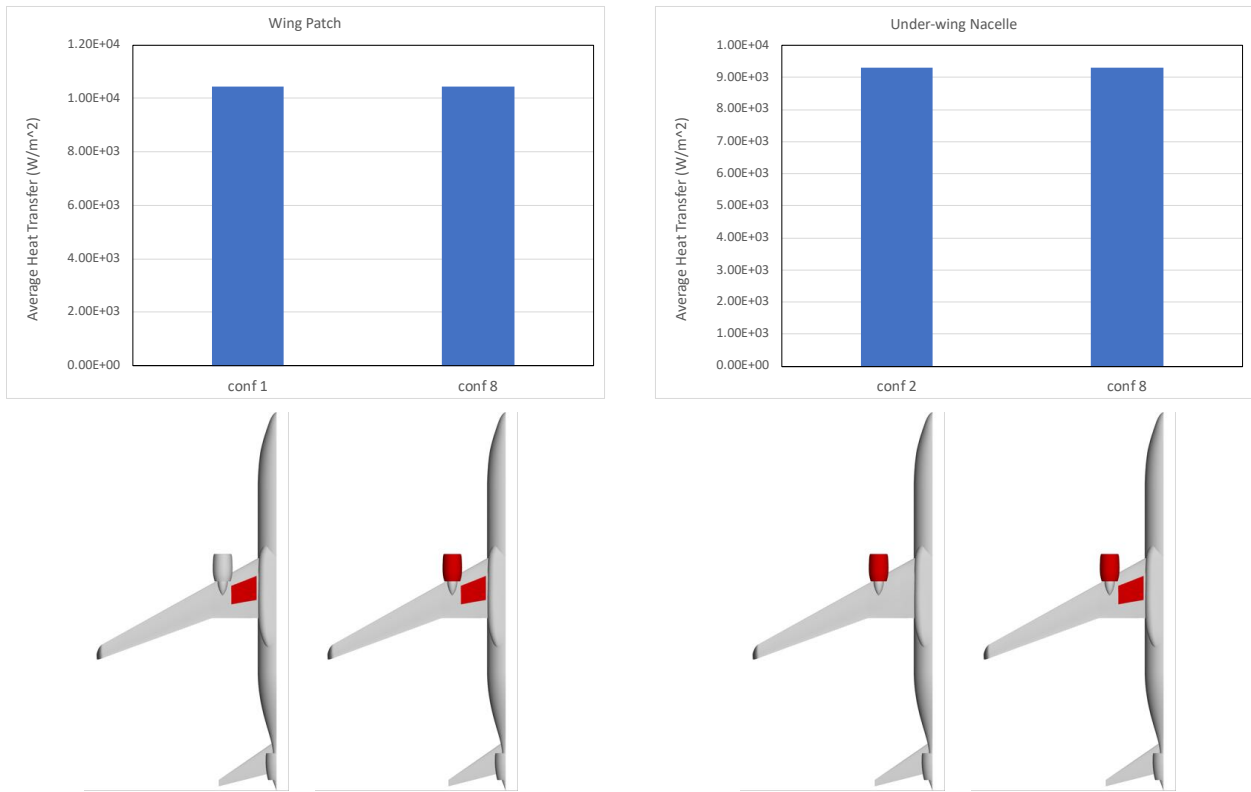
American Institute of Aeronautics and Astronautics

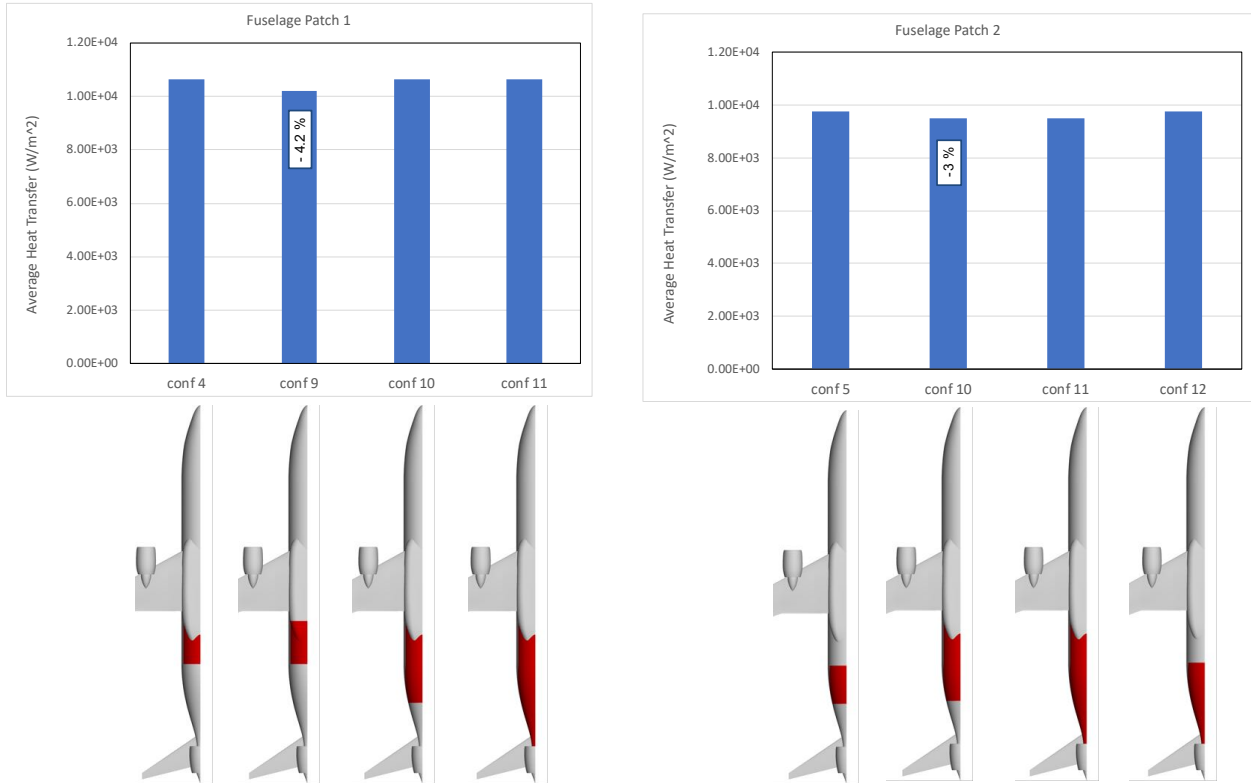Figure 13: Sensitivity of heat flux to OML patch configurations for STARC-ABL (cruise at $\alpha = 2°$).

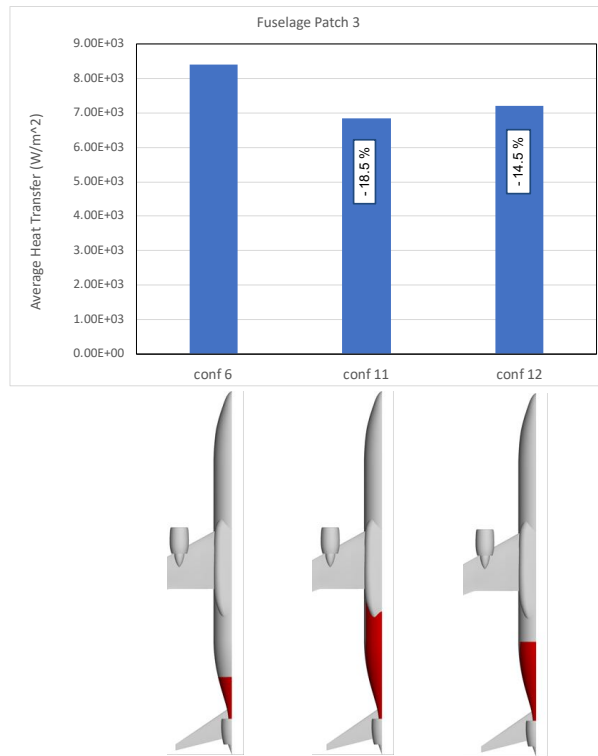Figure 14: Sensitivity of heat flux to OML patch configurations for STARC-ABL (cruise at $\alpha = 2°$).

Figure 15: Sensitivity of heat flux to OML patch configurations for STARC-ABL (cruise at $\alpha = 2°$).

III.A.5. Effect on Vehicle Aerodynamics

Figure 16 shows the sensitivity of aerodynamic forces with respect to the OML cooling patch configurations as illustrated on the left of the figure. We were particularly interested in potential drag reduction with the application of OML heat exchanger at the fuselage tail cone sections where introduction of heat to the boundary layer may help energize the flow under an adverse pressure gradient. This effect can actually be observed for configurations 5, 6, 10, 11 and 12, each registering an improvement in lift to drag ratio. However the overall magnitude of the effect on aerodynamic forces were less than 0.2% in all measures and hence this effect is deemed insignificant.
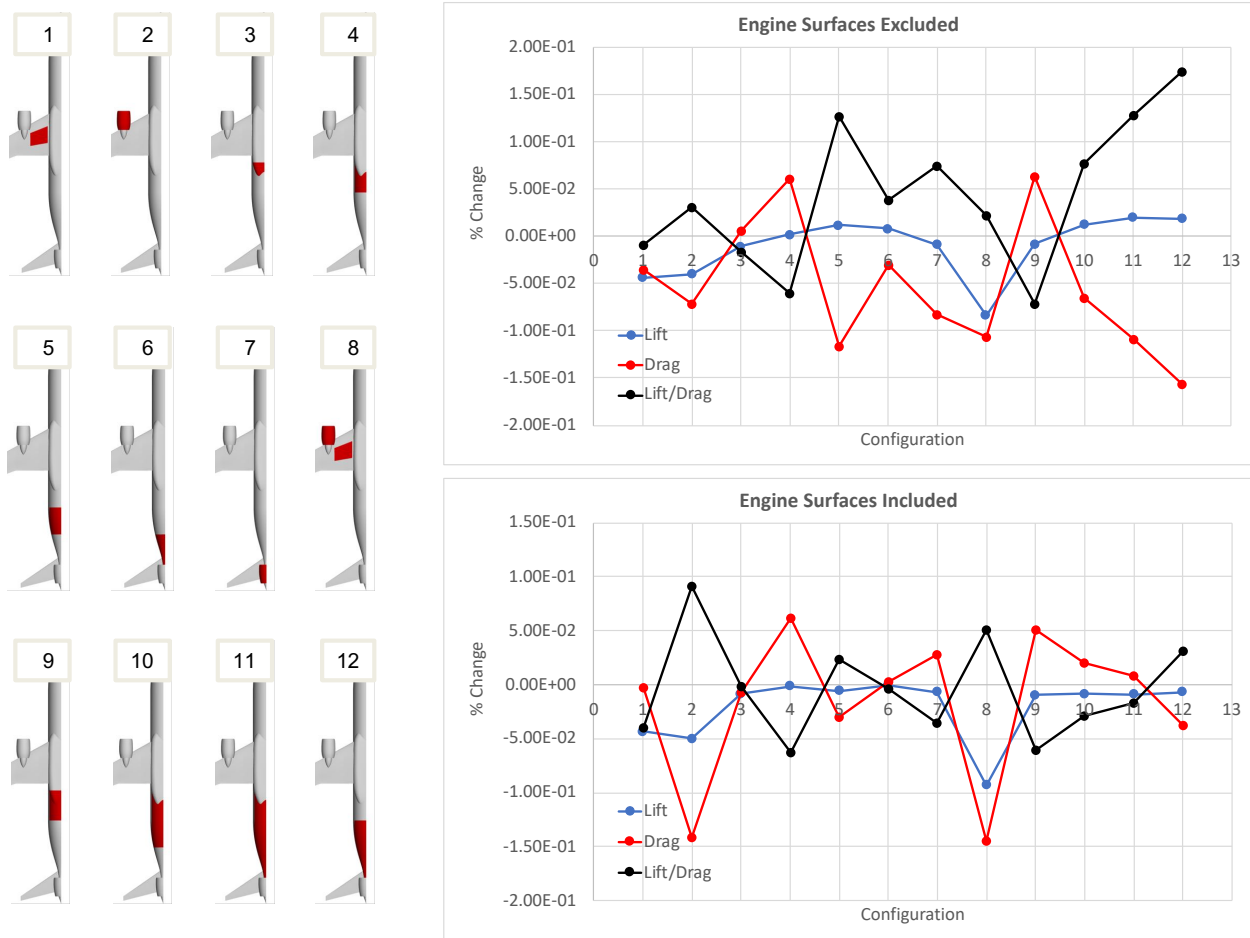
American Institute of Aeronautics and Astronautics

Figure 16: Sensitivity of aerodynamics loads to OML cooling patch selection for STARC-ABL (cruise at $\alpha = 2°$).

III.A.6.   Final STARC-ABL Results

With observations from the preliminary CFD analysis and the sensitivity studies, a final set of cruise and take-off condition CFD simulations were performed for STARC-ABL as listed in Table 1. Note that these simulations now include the effect of both the underwing and tail cone thrusters. In addition to preliminary analysis, take-off condition was also simulated for a hot day (40°C). Tables 2 and 3 list the final patch-averaged OML heat rejection results at cruise and take-off conditions consecutively. These results were used in downstream vehicle design analysis in sizing and weight estimation of a conceptual, passive OML-based cooling system.

American Institute of Aeronautics and Astronautics

Table 1: Final CFD run conditions for STARC-ABL.

	Cruise	Take-off	Take-off (Hot Day)
Altitude (ft)	37280	0	0
Ambient Pressure (Pa)	21,442	101,325	101,325
Ambient Temperature (°C)	-56.5 (standard)	30 (standard + 15)	40
Flight Mach	0.785	0.2547	0.2547
Angle of Attack	2	4,6,8,10	8
Under Wing Thrust (N)	10680	65375	65375
Tail BLI Thrust (N)	5685	10504	10504

Table 2: Final STARC-ABL cruise results.

Cruise Condition		
Patch	area (m^2)	Average Heat Flux (kW/m^2)
Wing-lower	5.45	10.44
Under-wing nacelle	16.69	9.62
Fuselage 2	8.98	9.77
Fuselage 3	5.83	7.63
Tailcone nacelle	8.84	10.68

Table 3: Final STARC-ABL take-off results.

Take-Off Condition					
		Average Heat Flux (kW/m^2)			
Patch	area (m^2)	alpha = 4	alpha = 6	alpha = 8	alpha = 8 (40°C day)	alpha = 10
Wing-lower	5.45	9.92	9.77	9.64	7.99	9.53
Under-wing nacelle	16.69	9.32	9.22	9.14	7.59	9.11
Fuselage 2	8.98	8.76	8.88	8.94	7.41	8.96
Fuselage 3	5.83	5.54	5.63	5.67	4.70	5.67
Tailcone nacelle	8.84	9.92	9.92	9.84	8.16	9.71

III.B.   RVLT

Following the findings and the methodology established in studying STARC-ABL, an OML-based heat exchanger was studied for application to another concept vehicle within the HEATheR project, namely the Revolutionary Vertical Lift Technologies (RVLT) aircraft. The full set of sensitivity studies as shown for STARC-ABL was not repeated for RVLT, assuming the conclusions drawn there are largely applicable here.

RVLT is a unique vehicle capable of hovering with a tilted wing. This restricts the application of OML cooling patches to the wing surfaces only, because during a demanding sustained hover condition, the only significant air flow is over the wing due to propeller downwash. With this consideration, the candidate OML cooling patches are partitioned as shown in Figure 17. The patches cover the entire wing surface and the two motor nacelles. The wing surfaces are split into lower and upper, as well as leading edge, mid-chord and trailing edge sections along 3 span-wise sections.

The computational grid for RVLT has approximately 24 million arbitrary polyhedral elements as shown in Figure 18. Only half of the airplane is modeled, taking advantage of the symmetry. The first layer wall normal spacing is selected to result in a $y^+ < 1$ condition.

Table 4 lists the cruise and hover conditions simulated. Note that take-off is not looked at for RVLT, as hover is considered to be the critical condition for this vehicle.
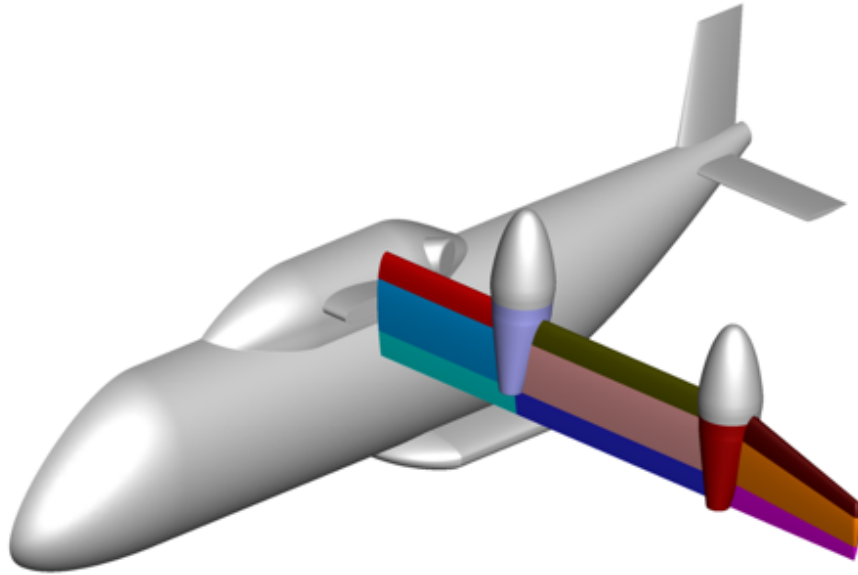
American Institute of Aeronautics and Astronautics
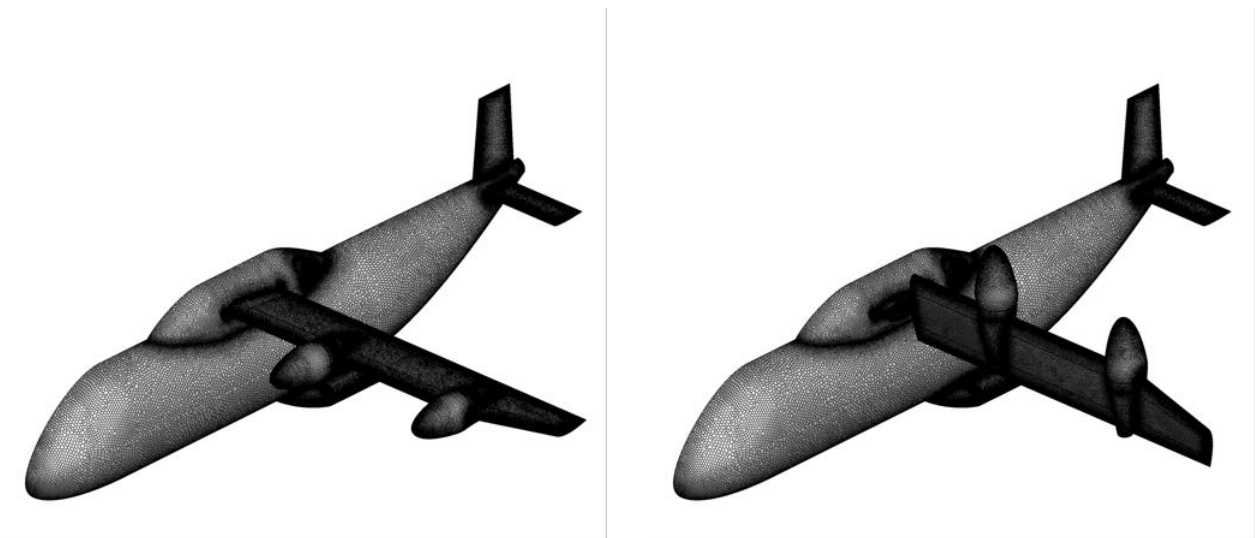
Figure 17: RVLT candidate OML cooling patches.

Figure 18: Arbitrary polyhedral unstructured grid for RVLT cruise (left) and hover (right).

Figure 19 shows the predicted heat flux distribution over the wing surface while the vehicle is hovering. We can clearly observe that the heat flux is distributed along bands roughly corresponding to the blade tip locations, and the effect is especially more pronounced in the mid-span where the inboard and outboard propeller blade tips overlap. Note that our propulsion modeling does not actually represent the propeller blades, but instead applies the total thrust output as a momentum source over a cylindrical control volume spanned by the rotation of the blades. While in this process, we could apply a spanwise blade load distribution, we did not have access to that loading distribution information at the time of the simulation, hence the loading is simply modeled as uniform. Considering that patch-averaged heat flux results (as seen in Figure 19 (right)) is an integral look, the results would likely be minimally affected by a different blade loading distribution. In terms of OML cooling patch implementation, the wing leading edges, motor nacelles and wing mid-chord patches offer a high capacity for heat rejection, especially for the mid-span section.

Figure 20 offers a look into hover in a 40°C hot day, as compared to the baseline (25°C day). For the

Table 4: RVLT CFD simulation conditions.

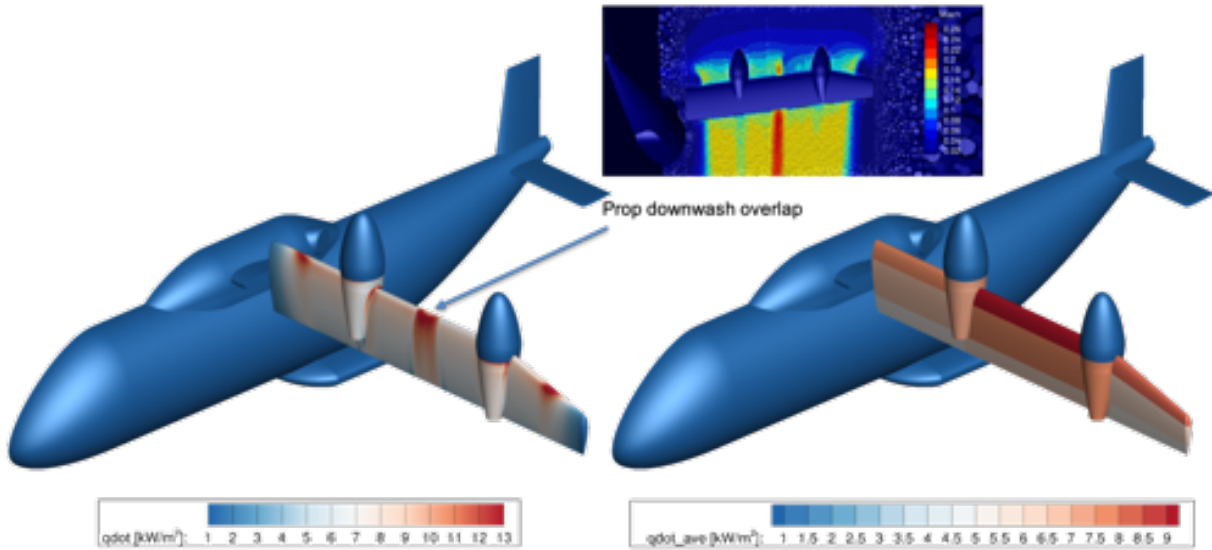|	**Cruise**	**Hover**	**Hover (Hot Day)**
Altitude (ft)	5000	5000	5000
Ambient Pressure (Pa)	84309	84309	84309
Ambient Temperature (°)	25.07 (standard + 20)	25.07 (standard + 20)	40
Flight Mach	0.297	0	0
Angle of Attack	0	0	0
Inboard Rotor Thrust (N)	1431	15407	15407
Outboard Rotor Thrust (N)	1431	15407	15407

Figure 19: RVLT at hover distributed (left) and patch-averaged (right) OML heat transfer.

hot day, the heat rejection capacity is reduced almost uniformly reduced by around 22%, which is directly in line to the reduction of OML skin temperature / ambient temperature differential.

Figure 21 and 22 shows the heat rejection capacity under cruise condition. Note that for these cruise simulations, the fuselage and tail surfaces were also modeled as isothermal in order to gain insight. However, only the wing surfaces are considered as implementation candidates due to the limiting hover case as discussed above. For cruise, the flight speed in addition to propeller wake results in a significantly higher heat rejection capacity as expected. Motor nacelles, wing leading edge and mid-chord patches all stand out as viable cooling surfaces.

Tables 5 and 6 list the patch-averaged heat flux values for the hover and cruise conditions, respectively.
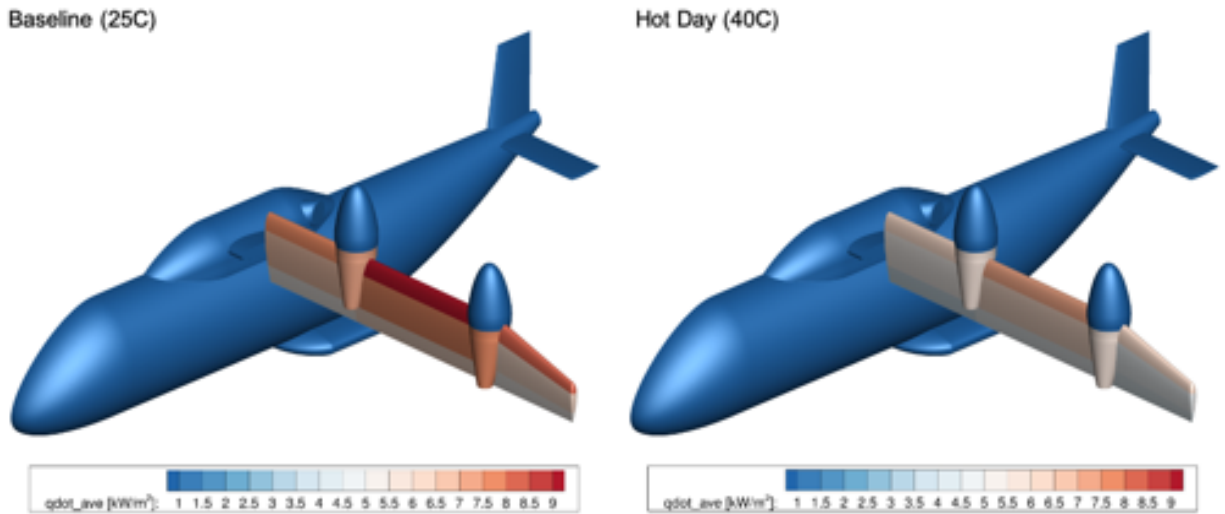
American Institute of Aeronautics and Astronautics

Figure 20: RVLT at hover heat transfer, baseline (left, 25°C) vs. hotday (right, 40°C).
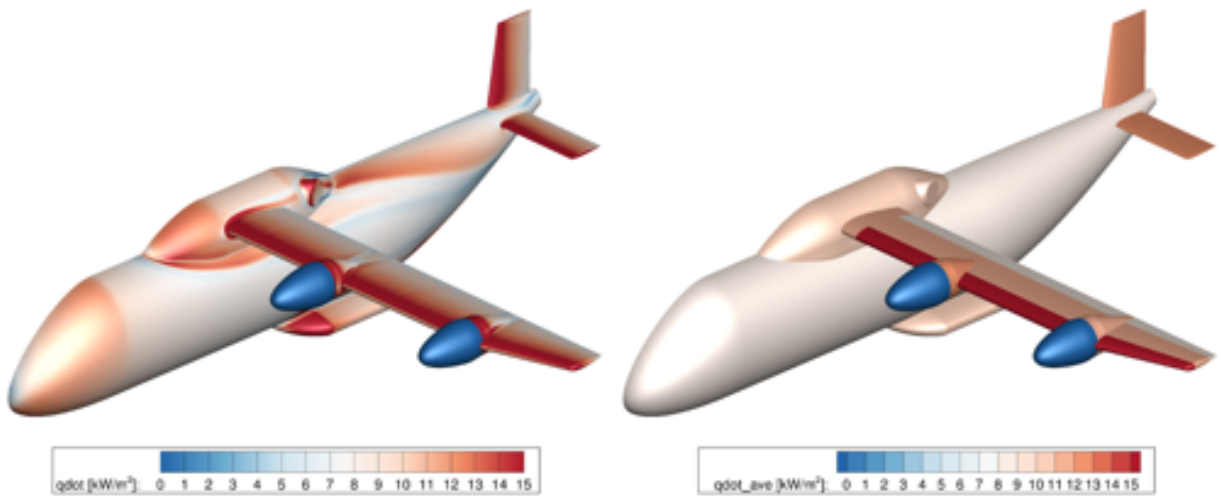

Figure 21: RVLT at cruise distributed (left) and patch-averaged (right) OML heat transfer, top.

Table 6: RVLT cruise CFD results.

| Cruise Condition		
Patch Name	**Area (m^2)**	**Average Heat Flux (kW/m^2)**
Leading Edge - Inboard	1.12	15.35
Leading Edge - Midboard	1.60	15.23
Leading Edge - Outboard	0.86	15.65
Mid-chord - Inboard (upper)	1.25	11.60
Mid-chord - Midboard (upper)	1.80	11.53
Mid-chord - Outboard (upper)	0.86	11.93
Mid-chord - Inboard (lower)	1.18	11.85
Mid-chord - Midboard (lower)	1.71	11.70
Mid-chord - Outboard (lower)	0.83	11.97
Nacelle - Inboard	1.37	12.42
Nacelle - Outboard	1.42	11.99
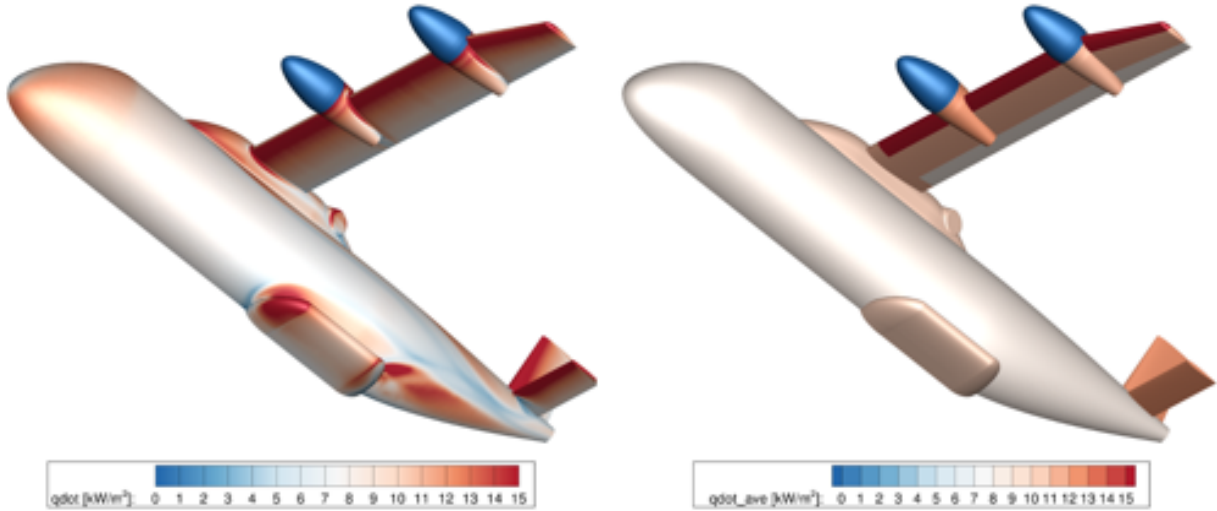
Figure 22: RVLT at cruise distributed (left) and patch-averaged (right) OML heat transfer, bottom.

Table 5: RVLT hover CFD results.

		Average Heat Flux (kW/m^2)	
Patch Name	**Area (m^2)**	*Baseline (25° C)*	*Hot Day (40° C)*
Leading Edge - Inboard	1.17	7.78	6.08
Leading Edge - Midboard	1.60	9.31	7.18
Leading Edge - Outboard	0.86	8.21	6.33
Mid-chord - Inboard (upper)	1.25	6.49	4.99
Mid-chord - Midboard (upper)	1.80	7.85	6.06
Mid-chord - Outboard (upper)	0.86	6.46	5.00
Mid-chord - Inboard (lower)	1.18	6.54	5.13
Mid-chord - Midboard (lower)	1.71	7.93	6.11
Mid-chord - Outboard (lower)	0.83	6.40	4.94
Nacelle - Inboard	1.37	7.50	5.79
Nacelle - Outboard	1.42	7.61	5.87

The **Hover Condition** header spans above the table as a title row.

III.C.   PEGASUS

The last vehicle considered within the HEATheR project is the Parallel Electric-Gas Architecture with Synergistic Utilization Scheme (PEGASUS). Like STARC-ABL, PEGASUS is a fixed-wing passenger aircraft concept, albeit smaller with a lower cruise altitude and speed. It is interesting to investigate if an OML-cooling scheme is versatile enough to be viable in this different flow regime as well. Table 7 shows the take-off and cruise conditions considered for PEGASUS.

The computational grid for PEGASUS has approximately 22.4 million arbitrary polyhedral elements as shown in Figure 23. Only half of the airplane is modeled, taking advantage of the symmetry. The first layer wall normal spacing is selected to result in a $y^+ < 1$ condition.

The OML candidate patches are split as shown in Figure 24. The wing surfaces are split in a similar manner to RVLT, i.e., in-board, mid-board and outboard, spanwise location that are further split into leading edge, mid-chord and trailing edge patches along approximately 1/4 and 3/4 chord locations. Motor nacelles are included as well. In addition, the wing-body joint fairing and lower tail-cone fuselage sections were included.

Heat flux results for take-off are shown in Figures 25 and 26. On the wing upper surface, expected

Table 7: PEGASUS CFD simulation conditions.

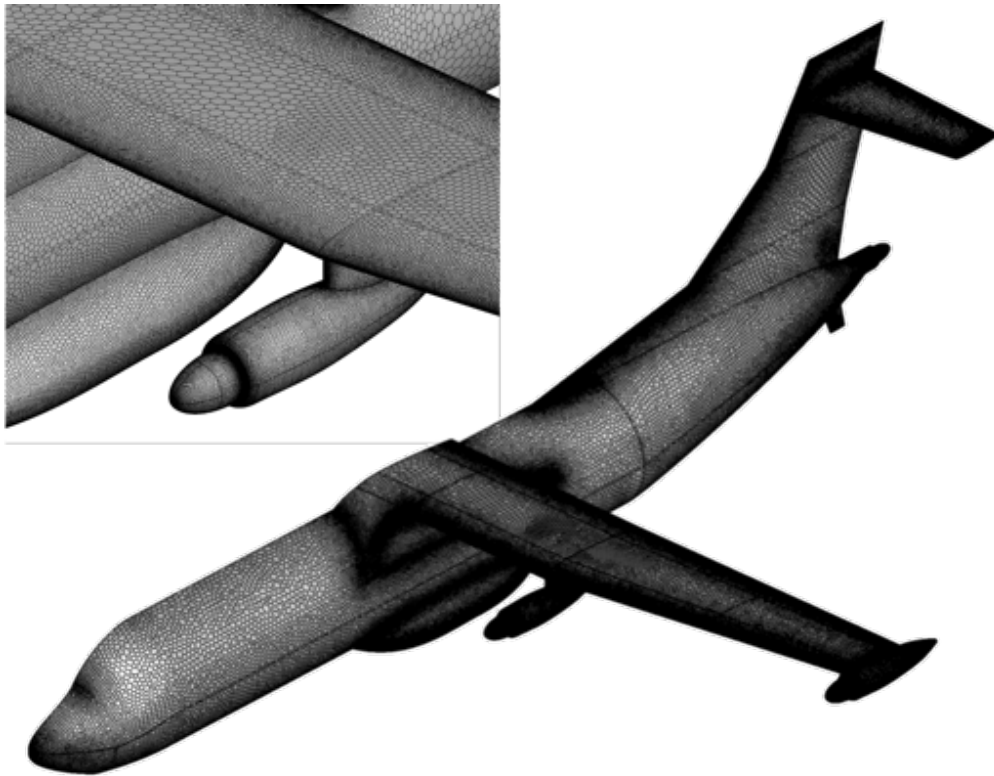|	Cruise	Take-Off	Take-Off (Hot Day)
Altitude (ft)	20,000	0	0
Ambient Pressure (Pa)	46,601	101,325	101,325
Ambient Temperature (°C)	-24.6 (standard)	33 (standard + 18)	40 (standard + 25)
Flight Mach	0.45	0.168	0.168
Angle of Attack (deg)	0	11	11
Inboard Rotor Thrust (N)	0	12099	12099
Outboard Rotor Thrust (N)	5654	8896	8896
Tailcone Thrust (N)	1223	6810	6810

Figure 23: Arbitrary polyhedral grid for PEGASUS.

behavior is apparent; the leading edge, mid-chord and motor nacelles all exhibit relatively high heat rejection capacities. The effect of propeller wake is also apparent, strengthening the heat transfer in patches directly downstream of the motors with the effect being stronger for the in-board motor (which has a significantly higher thrust than the outward motor for take-off, see Table 7). As also observed for STARC-ABL, at the high angle of attack take-off conditions, wing upper surfaces generally yield a higher heat transfer rate compared to the lower surface. This can be explained by the shifting of the stagnation line towards the lower surface and the acceleration of the flow over the upper surface at high angle of attack, attached flows. The tail cone fuselage patches seem to be less effective compared to wing surfaces, with the further aft portions performing progressively worse. However, these fuselage sections offer a much larger area and might still be viable candidates for implementation at least for the waste heat from components near the aft end.

For the hot dat (40°C) scenario, the heat rejection capacity reduces in proportion to the free-stream/OML skin temperature differential as observed in Figure 27.

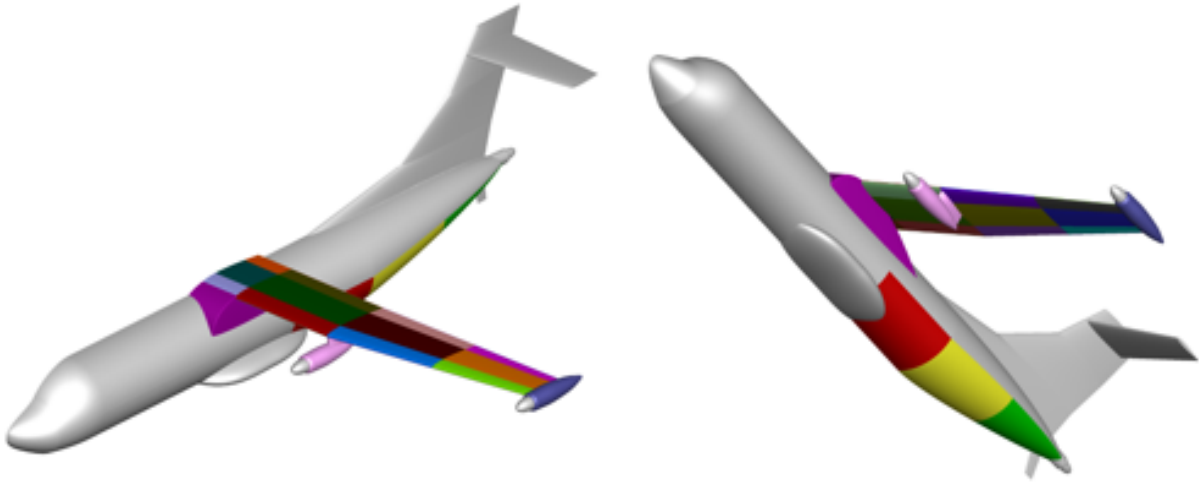American Institute of Aeronautics and Astronautics

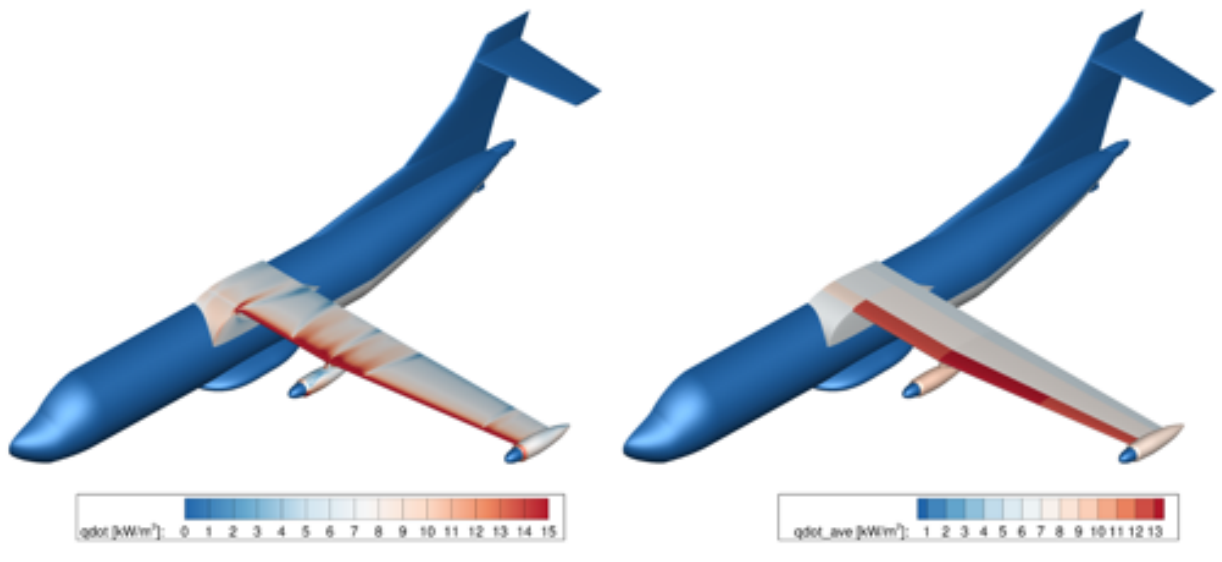Figure 24: PEGASUS candidate OML cooling patches.

Figure 25: PEGASUS at take-off distributed (left) and patch-averaged (right) OML heat transfer, top.

The heat transfer results for the cruise condition are shown in Figures 28 and 29. For cruise, consistently high heat rejection capacities are predicted for the leading edges and mid-chord patches as well as the motor nacelles. The patch-averaged results for both take-off and cruise conditions are tabulated in Tables 8 and 9, respectively.

IV.   Conclusions

Three different electrified aircraft concepts within HEATheR were considered for implementation of an OML-based heat exchanging scheme to reject the electrical component waste heat. CFD simulations for each vehicle were performed at different flight regimes, and the heat rejection capacity for various OML locations were predicted for an isothermal skin temperature of 200F. This particular skin temperature was chosen considering the limit at which both aluminum or composite skins can service long-term under stress.

The sensitivity of the heat rejection capacity predictions was studied in detail for STARC-ABL, looking into the effects of computational grid resolution, angle of attack variations and OML patch-to-patch inter-

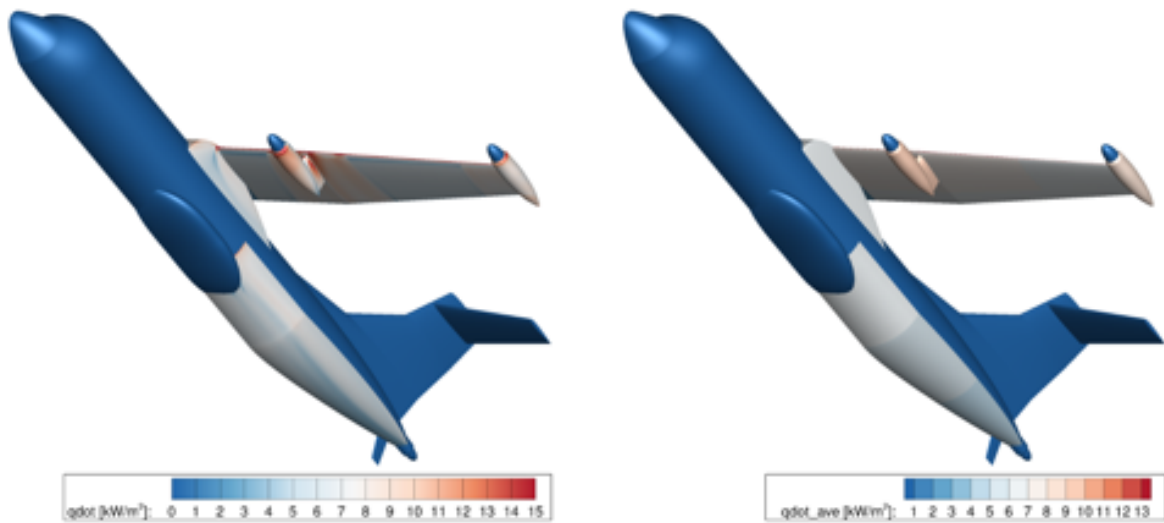American Institute of Aeronautics and Astronautics

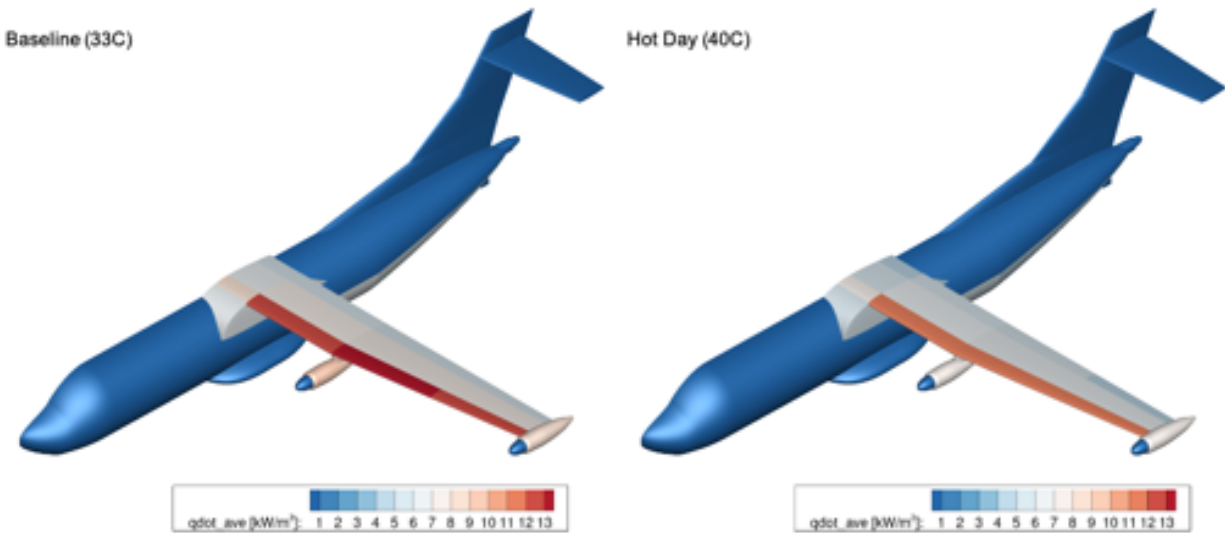Figure 26: PEGASUS at take-off distributed (left) and patch-averaged (right) OML heat transfer, bottom.

Figure 27: PEGASUS at take-off heat transfer, baseline (left, 33°C) vs. hotday (right, 40°C).

actions. The results were not largely sensitive to angle of attack variations or patch-to-patch interactions. In addition, the effect of OML-based cooling on vehicle aerodynamics was minimal.

For all three aircraft concepts, the heat rejection capacity was surprisingly consistent between take-off (or hover in the case of RVLT) and cruise conditions. The biggest difference was observed for PEGASUS for which the heat rejection capacity at cruise is generally double that of the take-off condition. At cruise altitudes, the ambient air temperature is much cooler than a typical sea-level take-off case but at sea level, the increased air density enhances the heat transfer. Luckily these two competing factors play a compensating role in helping equalize the performance of an OML-based heat exchanger at different flight conditions. However, the heat transfer at take-off (or hover) conditions is still more restricted, especially for a hot day. Considering that the take-off and hover also require a higher power draw (hence higher waste heat) compared to cruise, the former conditions are considered as critical for the sizing of an OML-based heat exchanger.

The CFD data produced in this work is used in the HEATheR project to decide the location and size of potential OML heat exchanger implementations. The penalty due to the system weight of these conceptual designs are compared to the combined drag and weight penalties of a traditional heat exchanger.

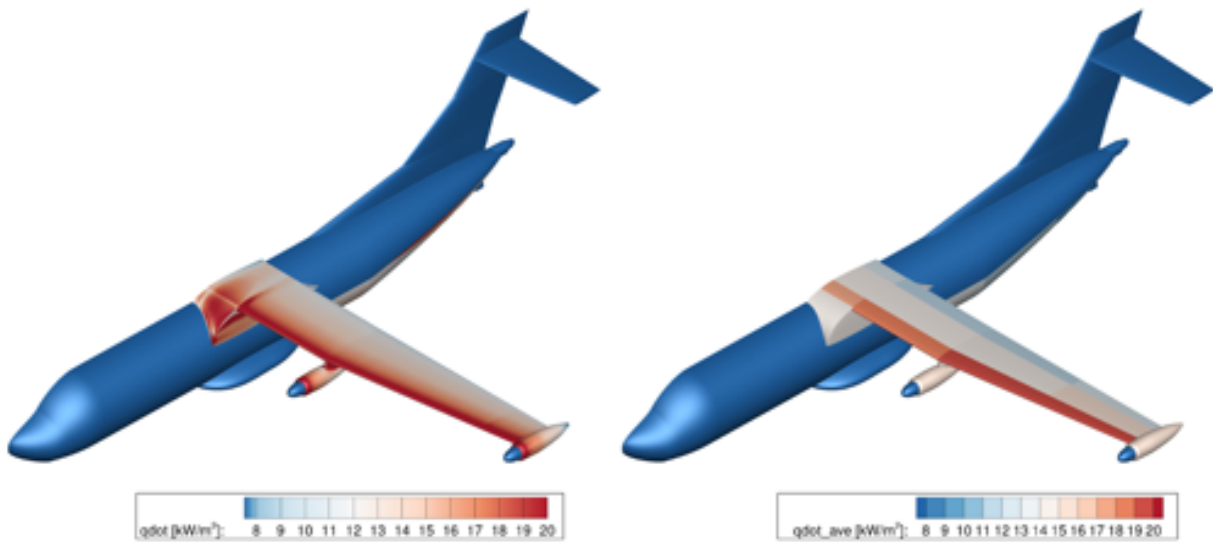American Institute of Aeronautics and Astronautics

Figure 28: PEGASUS at cruise distributed (left) and patch-averaged (right) OML heat transfer, top.
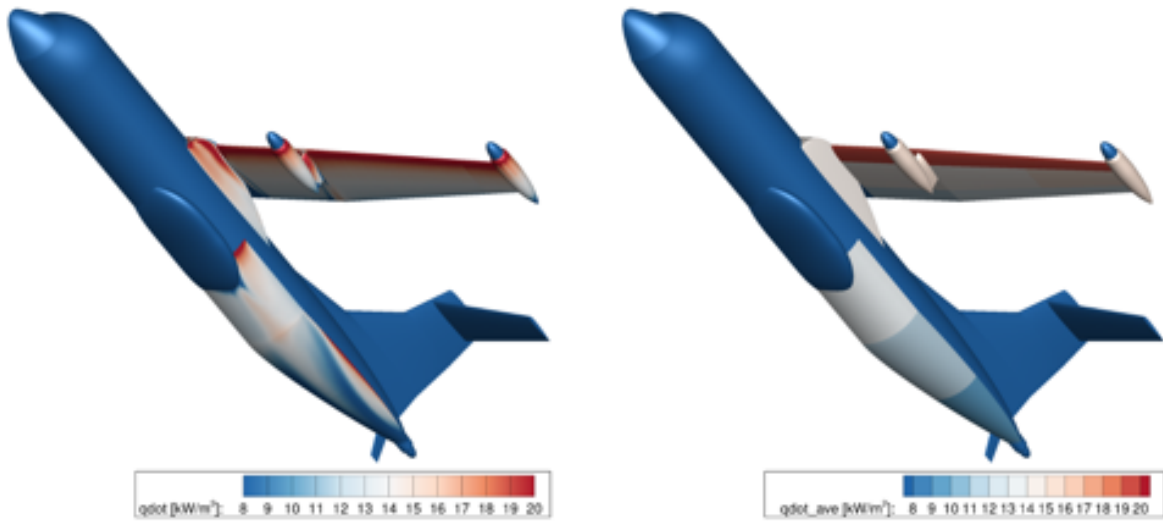

Figure 29: PEGASUS at cruise distributed (left) and patch-averaged (right) OML heat transfer, bottom.

The current work presented here is planned to be followed up with further verification and validation studies, by testing the CFD prediction capability used herein against experimental measurements utilizing a different CFD solver for repeat analysis for code-to-code verification.

In future design stages of these concept vehicles, the fidelity of the supporting CFD simulations can be increased by modeling the underlying structures of the OML-based heat exchanger in a conjugate simulation, hence replacing the uniform skin surface temperature assumption with a predicted distribution.

V.   Acknowledgements

American Institute of Aeronautics and Astronautics

Table 8: PEGASUS take-off CFD results.

Take-off Condition			
		Average Heat Flux (kW/m^2)	
Patch Name	**Area (m^2)**	**Baseline (33°C)**	**Hot Day (40°C)**
Fuselage 1	6.36	6.71	5.89
Fuselage 2	7.38	5.65	4.97
Fuselage 3	3.87	4.66	4.10
Wing Lower Outboard Mid	3.05	6.80	5.98
Wing Lower Outboard LE	1.51	6.82	6.00
Wing Lower Midboard LE	2.10	7.95	6.97
Wing Lower Inboard LE	2.21	7.66	6.72
Wing Lower Midboard Mid	4.28	7.52	6.59
Wing Lower Inboard Mid	4.53	7.43	6.51
Nacelle Inboard	4.21	9.11	7.98
Nacelle Outboard	3.56	8.16	7.17
Wing Upper Outboard Mid	3.04	7.39	6.49
Wing Upper Outboard LE	1.51	12.83	11.28
Wing Upper Midboard LE	2.15	13.05	11.45
Wing Upper Midboard Mid	4.33	7.90	6.92
Wing Upper Inboard Mid	4.60	7.86	6.89
Wing Upper Inboard LE	2.29	12.72	11.17

Table 9: PEGASUS cruise CFD results.

Cruise Condition		
Patch Name	**Area (m^2)**	**Average Heat Flux (kW/m^2)**
Fuselage 1	6.36	13.70
Fuselage 2	7.38	11.55
Fuselage 3	3.87	9.55
Wing Lower Outboard Mid	3.05	15.51
Wing Lower Outboard LE	1.51	19.90
Wing Lower Midboard LE	2.10	19.22
Wing Lower Inboard LE	2.21	19.03
Wing Lower Midboard Mid	4.28	14.82
Wing Lower Inboard Mid	4.53	14.24
Nacelle Inboard	4.21	15.73
Nacelle Outboard	3.56	15.37
Wing Upper Outboard Mid	3.04	15.49
Wing Upper Outboard LE	1.51	19.88
Wing Upper Midboard LE	2.15	19.03
Wing Upper Midboard Mid	4.33	14.72
Wing Upper Inboard Mid	4.60	14.71
Wing Upper Inboard LE	2.29	18.98

American Institute of Aeronautics and Astronautics

References

[1]Lents, C., "Parallel Hybrid Gas-Electric Geared Turbofan Engine Conceptual Design and Benefits Analysis," `https://ntrs.nasa.gov/search.jsp?R=20170000881`, 2016, [online].

[2]Garrett, M., "Development of an 11 kW Lightweight, High Efficiency Motor Controller for NASA X-57 Distributed Electric Propulsion Using SiC MOSFET Switches," *AIAA Propulsion and Energy Forum, Indianapolis, IN*, 2019.

[3]Welstead, J., "Overview of the NASA STARC-ABL (Rev. B) Advanced Concept," `https://ntrs.nasa.gov/search.jsp?R=20170005612`, 2017, [Online].

[4]Johnson, W., "Concept Vehicles for VTOL Air Taxi Operations," `https://ntrs.nasa.gov/search.jsp?R=20180003381`, 2018, [Online].

[5]Antcliff, K., "Conceptual Design of the Parallel Electric-Gas Architecture with Synergistic Utilization Scheme (PEGASUS) Concept," *18th AIAA/ISSMO Multidisciplinary Analysis and Optimization Conference, Denver, CO*, 2017.

[6]Kiris, C. C., Housman, J. A., Barad, M. F., Brehm, C., Sozer, E., and Moini-Yekta, S., "Computational framework for Launch, Ascent, and Vehicle Aerodynamics (LAVA)," *Aerospace Science and Technology*, Vol. 55, 2016, pp. 189 – 219.

[7]Brehm, C., Barad, M. F., Housman, J. A., and Kiris, C. C., "A comparison of higher-order finite-difference shock capturing schemes," *Computers & Fluids*, Vol. 122, 2015, pp. 184 – 208.

[8]Moini-Yekta, S., Barad, M., Sozer, E., Brehm, C., Housman, J., and Kiris, C., "Verification and Validation Studies for the LAVA CFD Solver," *21st AIAA Computational Fluid Dynamics Conference, San Diego, CA, AIAA–2013–2448, June 24-27*, 2013.

[9]Sozer, E., Brehm, C., and Kiris, C., "Gradient Calculation Methods on Arbitrary Polyhedral Unstructured Meshes for Cell-Centered CFD Solvers," *AIAA SciTech, National Harbor, Maryland, AIAA–2014–1440, Jan 13-17*, 2014.

[10]Kitamura, K. and Hashimoto, A., "Reduced dissipation AUSM-family fluxes: HR-SLAU2 and HR-AUSM+-up for high resolution unsteady flow simulations," *Computers & Fluids*, Vol. 126, 2016, pp. 41 – 57.

[11]Sapalart, P. R. and Allmaras, S. R., "A One-Equation Turbulence Model for Aerodynamic Flows," *Recherche Aerospatiale*, Vol. 1, 1994, pp. 5 – 21.

[12]Allmaras, S. R., Johnson, F. T., and Spalart, P. R., "Modifications and Clarifications for the Implementation of the Spalart-Allmaras Turbulence Model," *ICCFD7-1902, 7th International Conference on Computational Fluid Dynamics, Big Island, Hawaii, 9-13 July*, 2012.

American Institute of Aeronautics and Astronautics